RESEARCH ARTICLE Open Access

Singulonics: narwhal-shaped wavefunctions for sub-diffraction-limited nanophotonics and imaging

Wen-Zhi Mao[1†], Hong-Yi Luan[1†] and Ren-Min Ma[1,2,3*]

Abstract

The diffraction limit, rooted in the wave nature of light and formalized by the Heisenberg uncertainty principle, imposes a fundamental constraint on optical resolution and device miniaturization. The recent discovery of the singular dispersion equation in dielectric media provides a rigorous, lossless framework for overcoming this barrier. Here, we demonstrate that achieving such confinement necessarily involves a new class of optical eigenmodes—narwhal-shaped wavefunctions—which emerge from the singular dispersion equation and uniquely combine global Gaussian decay with local power-law enhancement. These wavefunctions enable full-space field localization beyond conventional limits. Guided by this principle, we design and experimentally realize a three-dimensional sub-diffraction-limited cavity that supports narwhal-shaped wavefunctions, achieving an ultrasmall mode volume of $5\times10^{-7}\,\lambda^3$. We term this class of systems singulonic, and define the emerging field of singulonics as a new nanophotonic paradigm—establishing a platform for confining and manipulating light at deep-subwavelength scales without dissipation, enabled by the singular dispersion equation. Building on this extreme confinement, we introduce singular field microscopy: a near-field imaging technique that employs singulonic eigenmodes as intrinsically localized, background-free light sources. This enables optical imaging at a spatial resolution of $\lambda/1000$, making atomic-scale optical microscopy possible. Our findings open new frontiers for unprecedented control over light–matter interactions at the smallest possible scales.

Keywords Singular dispersion equation, Narwhal shaped wavefunction, Singulonics, Singulonic nanocavity, Singularity, Singular field microscopy, Twisted lattice nanocavity, Power law enhancement

1 Introduction

In 1927, Dirac's revolutionary quantization of the electromagnetic field redefined our understanding of light, demonstrating that each electromagnetic mode can be treated as a quantum harmonic oscillator confined within a finite cavity [1]. When confined within a finite volume, electromagnetic modes become discrete and can be normalized, with their quantized energy levels corresponding to photons. This framework not only bridges the gap between quantized field modes and photonic excitations but also establishes the critical role of mode volume: smaller mode volumes increase the electric field per photon, thereby enhancing light–matter interactions. These principles form the cornerstone of cavity quantum electrodynamics [2–6], drive the evolution of advanced photonic technologies [7–43], and fuel the progression of modern quantum optics [44–46].

†Wen-Zhi Mao and Hong-Yi Luan have contributed equally to this work.

*Correspondence:
Ren-Min Ma
renminma@pku.edu.cn
[1] State Key Laboratory for Mesoscopic Physics and Frontiers Science Center for Nano-Optoelectronics, School of Physics, Peking University, Beijing, China
[2] Peking University Yangtze Delta Institute of Optoelectronics, Nantong, Jiangsu, China
[3] National Biomedical Imaging Center, Peking University, Beijing, China

Despite these advances, photonic devices continue to lag behind their electronic counterparts in terms of integration density and spatial resolution—a disparity rooted in the optical diffraction limit. In the visible and near-infrared regimes, the wavelength of photons is approximately three orders of magnitude larger than the de Broglie wavelength of electrons in electronic devices. This discrepancy imposes a fundamental constraint: the smallest achievable photonic mode volume is roughly nine orders of magnitude larger than the corresponding volume for electrons—nearly a billion times greater. Plasmonics has provided a means to overcome this diffraction limit, enabling significant breakthroughs in sensing, imaging, and on-chip photonics [7–21]. However, the unavoidable ohmic losses of metals remain a severe bottleneck, limiting their performance and scalability [17, 47, 48].

Achieving extreme photon confinement in a lossless system is essential for advancing photonic integration and imaging capabilities. Such a breakthrough would enable transformative applications that demand precise nanoscale control of light, including the optical observation of biomolecular structures such as DNA and the development of large-scale photonic integrated circuits with significantly enhanced processing speeds and efficiencies. Overcoming this challenge requires addressing a key limitation: achieving sub-diffraction-limited confinement in a lossless dielectric system.

Recent theoretical [22], numerical, and experimental advances [22–28] have introduced a promising new frontier in photonics: singulonics—a paradigm based on the singular dispersion equation in lossless dielectric media. This framework predicts power-law–divergent optical modes that enable sub-diffraction confinement in purely dielectric nanostructures, giving rise to what we term singulonic nanocavities [22]. However, these wavefunctions remain experimentally unverified, and their confinement is currently restricted to two spatial dimensions, falling short of achieving full three-dimensional (3D) confinement. Resolving this challenge presents a compelling opportunity to advance photonics, with the potential to unlock unprecedented capabilities in light manipulation and device performance.

In this work, we propose and experimentally demonstrate a singulonic cavity that enables deeply sub-diffraction-limited field confinement in all spatial dimensions. We show that singulonic confinement necessarily arises from a new class of optical eigenmodes—narwhal-shaped wavefunctions—which emerge from the singular dispersion equation and uniquely combine global Gaussian decay with local power-law enhancement. This hybrid profile enables sharp, full-space field localization beyond conventional limits. Guided by this principle, we design and fabricate a 3D singulonic cavity that supports these modes, achieving an ultrasmall mode volume of $5\times10^{-7}\ \lambda^3$—orders of magnitude below the diffraction limit. Using near-field scanning measurements, we directly probe the confined fields and provide the first experimental validation of singulonic wavefunctions in a lossless dielectric system, with results in excellent agreement with theoretical predictions and full-wave simulations. Building on this extreme confinement, we further introduce singular field microscopy: a near-field imaging technique that employs singulonic eigenmodes as intrinsically localized, background-free light sources. This enables optical imaging with a spatial resolution of $\lambda/1000$, making atomic-scale optical microscopy possible.

This work represents a key advance in the emerging field of singulonics—a nanophotonic paradigm rooted in the singular dispersion equation in lossless dielectric media, enabling deep-subwavelength light confinement and manipulation without dissipation. In contrast to plasmonics, which couples light to free electrons in metals and is fundamentally constrained by ohmic losses, singulonics employs purely dielectric nanostructures engineered to support narwhal-shaped wavefunctions. These so-called singulonic modes simultaneously achieve ultrasmall mode volumes and high optical quality factors, thereby overcoming the long-standing trade-off between confinement and loss.

2 Results

2.1 Narwhal-shaped wavefunction

The mode volume characterizes the effective spatial region in which an optical mode is confined. It is defined as the integral of the electric energy density over all space, normalized by its peak value. To minimize the mode volume, one must design the electromagnetic field to decay rapidly from its intensity maximum, thereby tightly concentrating the mode and enhancing the peak energy density.

Conventional optical modes typically follow a Gaussian-like intensity profile, $I(x) = I_0\exp\left(-\frac{x^2}{2\sigma^2}\right)$, where I_0 is the peak intensity at $x=0$, and σ defines the mode width. The local logarithmic gradient, defined as $\left|\frac{\mathrm{d}(\ln I)}{\mathrm{d}x}\right| = \frac{|x|}{\sigma^2}$ measures relative rate of intensity variation. While this gradient increases with distance from the center, it vanishes exactly at the peak. As a result, Gaussian modes exhibit too little variation near the intensity maximum to achieve strong confinement, fundamentally limiting their ability to minimize the mode volume.

Power-law profiles, such as $|\mathbf{E}|^2 \propto r^{-2l}$, offer a complementary behavior. Their logarithmic gradient, $\frac{2l}{r}$, increases as $r\to0$, enabling sharp localization near the center. However, these modes decay too slowly at large

distances, resulting in extended spatial tails that compromise overall confinement.

To overcome these opposing limitations, we introduce a hybrid wavefunction that combines the sharply peaked core of a power-law profile with the rapidly decaying tail of an exponential function (Fig. 1). This composite form maintains strong field variation across all spatial scales and significantly reduces the total mode volume (Fig. 1b–d; Fig. S1 in the Supplemental Material). Owing to its resemblance to the tapering profile of a narwhal's head, we refer to this optimized field distribution as the narwhal-shaped wavefunction.

While conventional dielectric cavities typically support Gaussian-like modes, realizing the narwhal-shaped wavefunction requires the introduction of a power-law singularity at the field maximum, carefully matched to the global mode properties. In our implementation, a twisted lattice cavity provides the global confinement background, chosen for its ability to support smoothly varying, high-quality-factor (high-Q) modes with a broadly Gaussian envelope (Fig. 1e) [42]. In principle, other cavity geometries can fulfill a similar role.

To produce the required power-law enhancement near the field maximum, we embed a dielectric biconical antenna at the center of the cavity. This 3D tapering structure induces power-law scaling of the electric field in all spatial directions near its apex, effectively generating a localized singular core (Fig. 1f). The resulting field profile naturally bridges the smooth, large-scale confinement imposed by the cavity and the sharp, localized concentration introduced by the antenna.

The resulting mode is the eigenmode of the integrated structure—a composite singulonic cavity that combines global and local confinement in a synergistic manner. The twisted lattice ensures effective spatial confinement and suppression of radiative loss, while the biconical antenna introduces a geometric singularity that tightly concentrates the field. Together, these two elements give rise to the narwhal-shaped wavefunction, enabling robust 3D, deep-subwavelength localization of light in a fully dielectric and intrinsically lossless platform.

2.2 Three-dimensional singular field

We find that a dielectric biconical antenna supports a 3D singular field, which rapidly diverges following a power law in all spatial dimensions as it approaches the apex singularity of the conical dielectric structures (see Sect. 4.1; Supplemental Material for more details). Near the singularity (where $k_0 r \ll 1$, with k_0 being the free space wavevector and r representing the distance from the apices in spherical coordinates), the eigen-wavefunction is given by $\mathbf{E}_s = C_s r^{-l} \mathbf{\Theta}(\theta, \varphi)$, where C_s is a constant, l is a constant between 0 and 1, $\mathbf{\Theta}(\theta, \varphi)$ is a function of the spherical coordinate angles θ and φ.

This 3D singular field indicates that the electric field varies with the distance r from the singularity following a power law with exponent l in any spatial direction defined by the angles θ and φ. This scaling law allows the electric field to vary by several orders of magnitude within a subwavelength range (Fig. 1; Fig. S1 in the Supplemental Material), serving as a fundamental mechanism for overcoming the optical diffraction limit in dielectric systems.

As $r \to 0$, the electric field diverges, tending toward infinity. In dielectric systems, this field divergence corresponds to a divergence of the mode wavevector. Physically, the wavevector characterizes the spatial variation of the field—larger wavevectors correspond to finer spatial features. For any polarization component of the electric field, we can define a position-dependent wavevector by rewriting the field expression from $E(r, \theta, \varphi) = e^{i\mathbf{k}(r,\theta,\varphi)\cdot\mathbf{r}}$ to $E(r, \theta, \varphi) = e^{i\int \mathbf{k}(r,\theta,\varphi)\cdot d\mathbf{r}}$. This formulation allows us to incorporate the spatially varying wavevector associated with the power-law behavior and derive the corresponding dispersion equation. In this regime, the power-law-scaled electric field causes all components of the wavevector to diverge as $\frac{1}{r}$ [see Equation (19) in Supplemental Material]. The resulting dispersion relation takes the form:

$$(ik_r)^2 + k_\theta^2 + k_\varphi^2 - i\left(\frac{\partial}{\partial r} + \frac{2}{r}\right)(ik_r) - i\frac{1}{r}\left(\frac{\partial}{\partial \theta} + \cot\theta\right)k_\theta - i\frac{1}{r\sin\theta}\frac{\partial}{\partial \varphi}k_\varphi \approx \left(\frac{n\omega}{c}\right)^2,$$

where ik_r, k_θ, and k_φ are wavevectors along r-, θ-, and φ-directions, respectively, k_r is a real number. Here, n is the

(See figure on next page.)

Fig. 1 Narwhal-shaped wavefunction—A hybrid optical field profile that combines a steep power-law decay near its intensity peak with a rapidly vanishing Gaussian-like tail. This dual behavior accelerates field attenuation across the entire domain, enabling exceptionally small mode volumes and giving the profile its resemblance to a narwhal's head. **a** Narwhal sketch. **b** Log-scale 2D intensity distribution of a narwhal-shaped wavefunction. **c** 1D intensity distribution of a narwhal-shaped wavefunction along *x*-axis. **d** Local logarithmic gradient of the electric field intensity with respect to position. **e** A twisted lattice cavity supports a high-*Q* Gaussian-like mode. **f** Introducing a biconical antenna at the twisted lattice cavity center gives rise to the narwhal-shaped wavefunction that preserves the cavity's global confinement while exhibiting a sharp power-law enhancement near the center

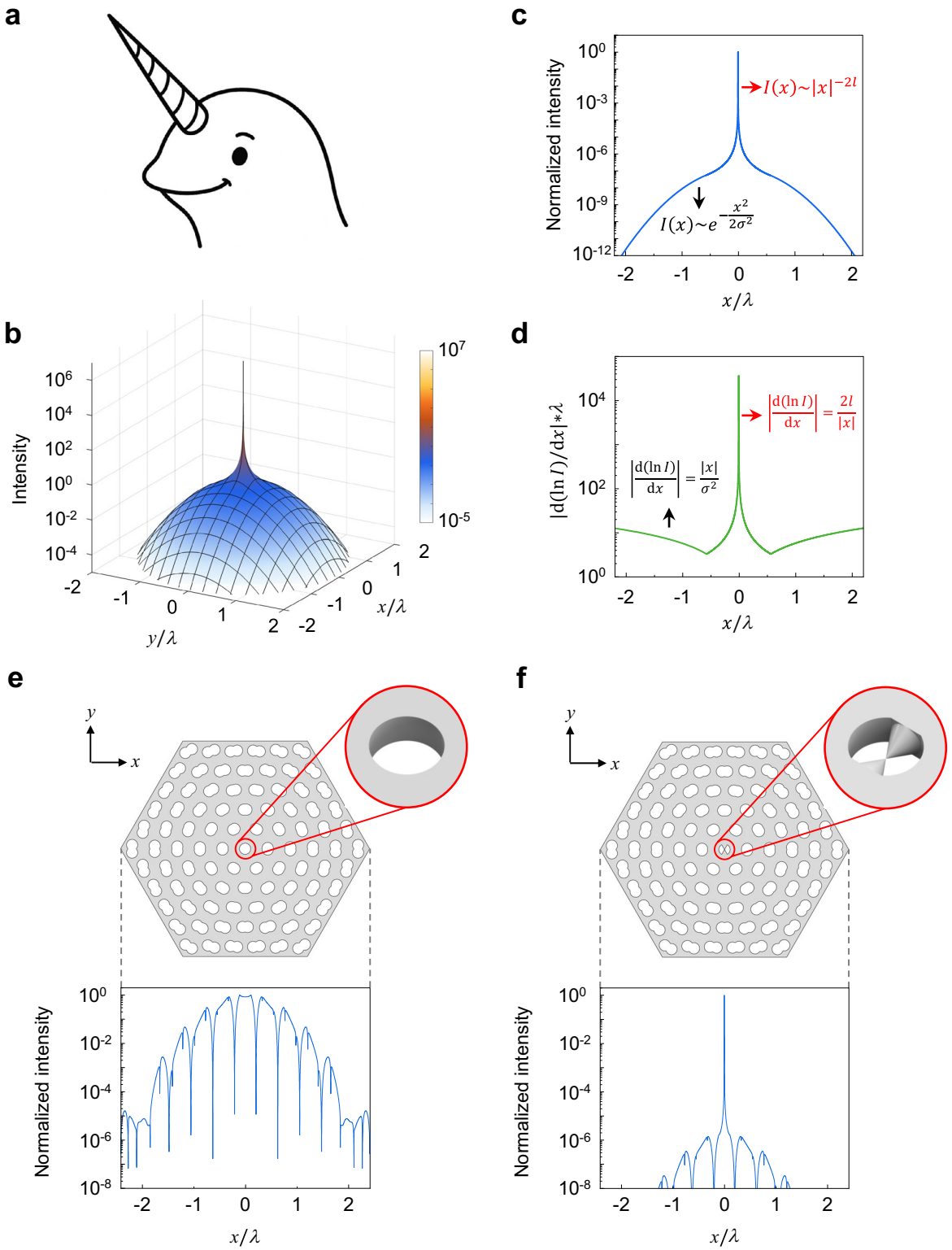

Fig. 1 (See legend on previous page.)

refractive index of the region described by the dispersion relation, ω is the angular frequency, and c is the speed of light in vacuum.

We note that as $r \to 0$, all terms on the left-hand side of the dispersion equation diverge but cancel each other. Among the three wavevector components, the radial component is purely imaginary—analogous to the imaginary transverse wavevector in plasmonics, but without metallic loss. As $r \to 0$, this component diverges, reflecting a field that decays rapidly as r increases in all directions. This divergence drives all wavevector components governed by the dispersion equation to approach infinity, thereby enabling the electric field to achieve extraordinary localization in real space across all spatial dimensions.

As $r \to 0$, the magnetic field strength becomes a higher-order small quantity compared to the electric field. However, when $k_0 r$ is no longer much smaller than one, the magnetic field no longer vanishes, resulting in an outward energy flow from the singularity. This behavior explains why dielectric antennas alone cannot support sub-diffraction-limited modes and inherently suffer from extremely low quality factors (Fig. S2 in the Supplemental Material). In contrast, in the construction of the narwhal-shaped wavefunction, the emergence of a non-negligible magnetic field naturally facilitates the matching of boundary conditions between the two distinct spatial regions of the mode—enabling both deep subwavelength confinement and a high quality factor.

2.3 Experimental characterization of narwhal-shaped wavefunction

We have developed a 3D singulonic cavity operating in the microwave band (~1.3 GHz), enabling precise, direct, 3D measurements of its eigen-wavefunction. Figure 2a shows the singulonic cavity, which comprises a 3D biconical antenna and a twisted lattice cavity (see Sect. 4.2). Both components are made of dielectric materials: the twisted lattice cavity is formed from aluminum oxide, while the biconical antenna is fabricated from zirconium oxide.

In the twisted lattice cavity, the twist angle is 3.89°, and the lattice constant for both sets of identical photonic graphene lattices is 100 mm ($\sim\lambda/2$). The biconical antenna is composed of two zirconium oxide cones, separated by an air gap of approximately 0.02 mm ($\sim 9\times10^{-5}$ λ), enabling extreme electromagnetic field localization at the singularity. Zirconium oxide was selected for its higher dielectric constant, which increases the power-law exponent l, thereby amplifying the rate of change of the electric field in regions governed by the power-law profile.

Figures 2 and 3 show both the 3D full-wave simulated and experimentally measured sub-diffraction-limited wavefunctions of the singulonic cavity. Figure 2b highlights the mode's 3D field distribution, along with two-dimensional (2D) projections onto the x–y, x–z, and y–z planes. Figures 2c, d and 3c further present cross-sectional field profiles (lines) taken through the singularity in each of the three projected field distributions, alongside the corresponding experimental results (dots) (see Sect. 4.3; Figs. S3, S4 in the Supplemental Material). All three cross sections exhibit a distinct narwhal-shaped profile, and the experimentally measured field distribution matches well with the simulation.

Figures 2e, f and S5 in the Supplemental Material compares the simulated and experimentally measured electric field near the singularity. The field intensity peaks at the singularity and decays outward following a power law of approximately $r^{-0.9}$, in excellent agreement with the simulations (see Fig. S6 in the Supplemental Material). This strongly localized field, which exhibits a power-law decay in all spatial directions, arises from the diverging imaginary radial wavevector. Figure 3b shows normalized magnetic-to-electric field amplitude ratio in the same region as the electric field plotted in Fig. 3a. The ratio remains small across the domain but gradually increases with distance from the singularity. At the wavelength scale, it becomes comparable to the electric field strength.

Notably, strong localization—and thus an ultra-small mode volume—emerges well before $r=0$, governed by power-law scaling as r decreases, rather than by a strict mathematical singularity (see Fig. S7 in the Supplemental Material). The simulations were performed using the actual device geometry, including the biconical antenna structure. The experimentally observed field enhancement is lower than the simulated result, primarily due to the finite size of the probe antenna, which prevents it from accessing the apex region where the field is most concentrated.

In the 2D cross section of this 3D field, the phase varies sharply near $r=0$ along the φ-direction, indicating a diverging angular wavevector k_φ [Fig. 4; see also the discussion of mode decomposition in Supplemental Material, Equations (16)–(17)]. Such rapid angular phase variation (diverging real angular wavevector) causes the pronounced radial field decay (imaginary radial wavevector), consistent with the dispersion equation. Figure 4b shows the directly measured phase shift around the singularity, again in excellent agreement with the simulations. Due to the unique narwhal-shaped wavefunction, the mode volume of the singulonic cavity is minimized. 3D full-wave simulations indicate that its mode volume is 5×10^{-7} λ^3 (see Sect. 4.4; Figs. S8–S11 in the Supplemental Material), exceeding that of previously reported 2D

(See figure on next page.)

Fig. 2 Experimental characterization of a 3D narwhal-shaped wavefunction. **a** Photograph of a singulonic cavity supporting a 3D narwhal-shaped wavefunction. The cavity incorporates a biconical antenna and a twisted-lattice structure. Bottom insets: enlarged views of the biconical antenna region. **b** 3D full-wave simulation of the cavity's eigen-wavefunction, showing the mode's 3D field distribution along with its 2D projections on the *x*–*y*, *x*–*z*, and *y*–*z* planes. **c**,**d** Cross-sectional electric field profiles taken through the singularity along the *x*-direction ($y=0, z=0$) and *y*-direction ($x=0$, $z=0$), respectively. **e**,**f** Magnified views of (**c**) and (**d**), respectively, to resolve the steep field enhancement near the singularity. Due to measurement limitations, experimental values along *x*-direction near the singularity are measured at $z=0.002\,\lambda$, while those in the *y*-direction are measured along the side of the biconical antenna in *x*–*y* plane at $z=0$. Outside the biconical antenna area, field values ($|x|, |y| > 0.11\,\lambda$) are obtained at the cavity surface ($z=0.06\,\lambda$). Solid lines: simulation results; circles: experimental measurements; dashed lines: Gaussian functions for reference

singulonic cavities by nearly three orders of magnitude [22, 26–28].

2.4 Extending to the optical regime

The narwhal-shaped wavefunction field localization mechanism demonstrated here is scale-invariant and, in principle, extendable to optical frequencies. Figure 5 shows preliminary results on the fabrication of a singulonic nanocavity operating in the optical regime, along with its simulated electric field distribution. With continued optimization, this approach could realize fully 3D, sub-diffraction-limited nanocavities with atomic-scale feature sizes—unlocking new possibilities for nanophotonic integration, quantum light–matter interaction, and atomic-resolution optical imaging.

2.5 Singular field microscopy

Leveraging the uniquely confined field defined by the narwhal-shaped wavefunction, we introduce singular field microscopy—a new approach to near-field scanning optical microscopy (Fig. 6). In contrast to conventional aperture- or scattering-based techniques [49–52], this approach exploits the extreme confinement and purity of singulonic eigenmode to directly probe deeply subwavelength features. Structural perturbations from the sample modulate the resonance of the singulonic eigenmode, allowing high-fidelity readout of deep subwavelength details through measurable spectral shifts.

In our implementation, an air gap of approximately 0.2 mm ($\sim\lambda/1100$) is formed between the two dielectric antennas. The sample is positioned within the gap of the biconical structure and scanned in a plane perpendicular to the antenna axis (Fig. 6a; see Sect. 4.3; Fig. S12 in the Supplemental Material). As the sample translates, local variations in its dielectric environment perturb the resonance frequency of the cavity. By raster-scanning the sample in two dimensions, the singular field is swept across its surface, and the resonance spectrum is recorded at each position, producing a spatially resolved map of subwavelength features. Owing to the extreme field localization, singular field microscopy enables the detection of structural details far beyond the diffraction limit.

To explore how different materials affect the cavity's resonance frequency, we prepare thin films (approximately $\lambda/2300$ in thickness) using three materials with distinct refractive indices—polyethylene terephthalate (PET), aluminum oxide, and zirconium oxide—and place them within the air gap (Fig. S13 in the Supplemental Material). The results indicate that higher refractive index induces a more pronounced effect on the resonance frequency. In the further imaging experiments, we select PET, whose refractive index is close to that of air (around 1.7), and fabricate perforated patterns on its surface for scanning. The minimal refractive index contrast between PET and air highlights the sensitivity of the singulonic cavity's resonance frequency to changes in material properties, underscoring its potential for imaging applications.

We perform line-profile analysis to evaluate the resolution of singular field microscopy. First, we image two closely spaced PET strips separated by $0.95\times10^{-3}\ \lambda$ (Fig. 6b). The resulting two peaks were distinctly resolved, confirming the technique's ability to distinguish nearby features. Next, to test the line resolution, we scan a dielectric strip measuring only $0.37\times10^{-3}\ \lambda$ in width; the acquired profile exhibited a full width at half maximum (FWHM) of $0.95\times10^{-3}\ \lambda$ (Fig. 6c). These measurements confirm that singular field microscopy achieves a resolution better than $1\times10^{-3}\ \lambda$. Figure S14 in the Supplemental Material provides additional line-profile analysis of a dielectric–air interface, and Fig. S15 in the Supplemental Material shows line profiles of single strips with various widths and two-strip configurations with different gap sizes. Collectively, these findings underscore the high-resolution capabilities of singular field microscopy.

Singular field microscopy can also image arbitrary structures at deeply sub–diffraction-limited resolutions (Fig. 7). We used it to examine two perforated dielectric PET samples patterned with "PKU" and "SFM", where each letter stroke measures less than $1\times10^{-3}\ \lambda$ in width (Fig. 7a). The resulting images confirm that this technique

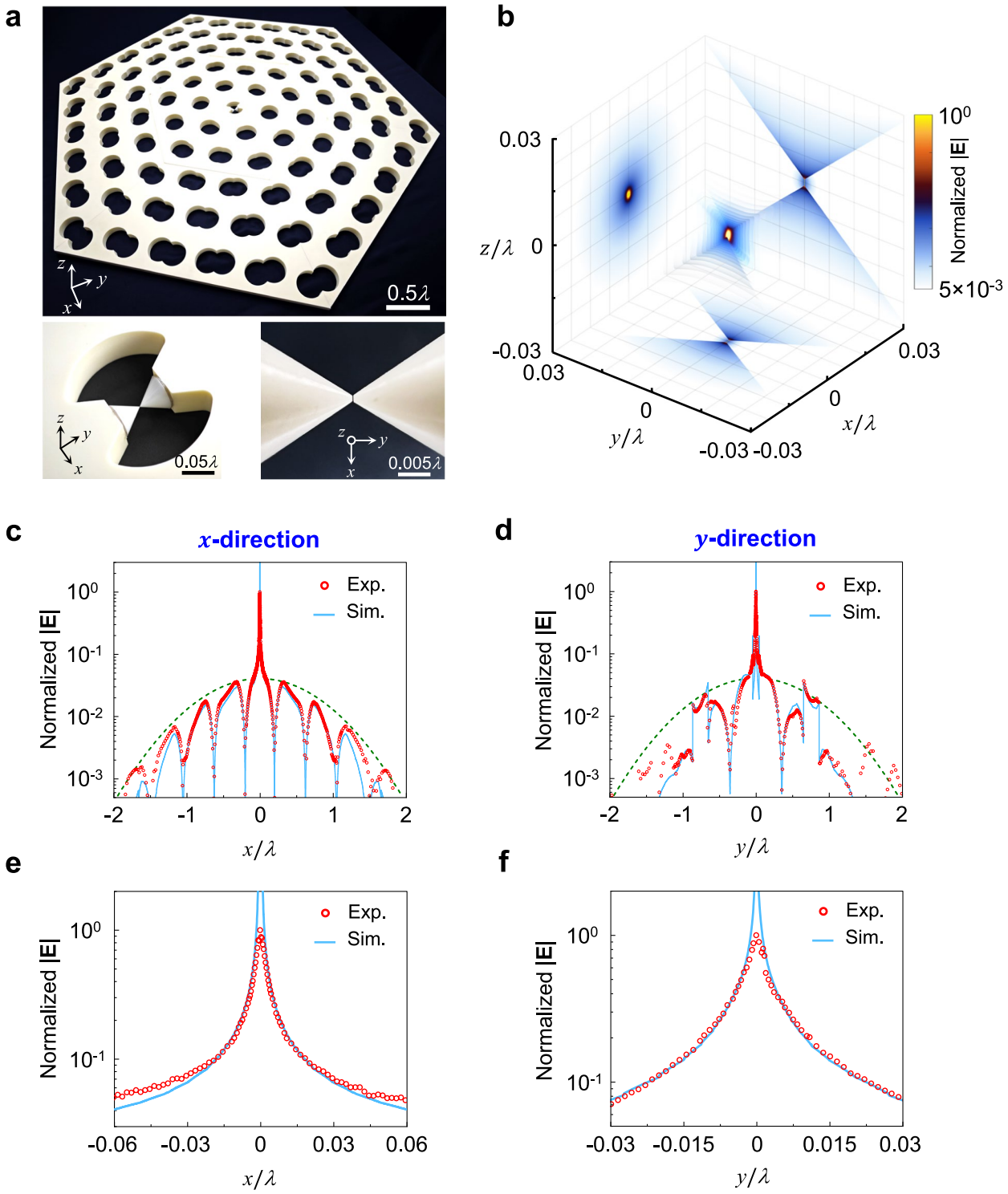

Fig. 2 (See legend on previous page.)

faithfully reproduces intricate structural details in all directions with high fidelity (Fig. 7b–e).

3 Discussions

We experimentally realize a singulonic cavity that achieves full-space, deeply subwavelength field confinement with an ultrasmall mode volume of 5×10^{-7}

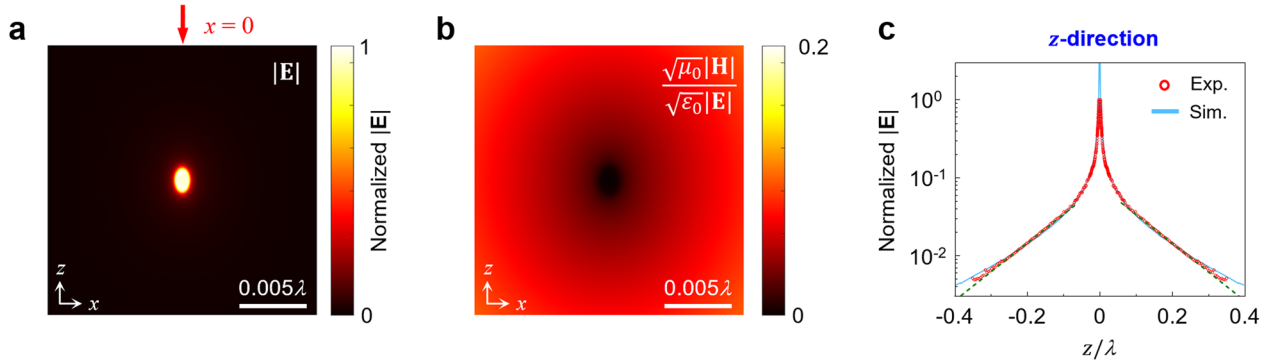

Fig. 3 Simulated electromagnetic field and experimentally measured electric field along *z*-direction. **a** Simulated electric field distribution in the *x*–*z* plane at $y=0$. **b** Simulated spatial distribution of the normalized magnetic-to-electric field amplitude ratio in the *x*–*z* plane at $y=0$. The ratio remains small throughout the domain but increases away from the central singularity. **c** Comparison of simulated and experimentally measured electric field at $x=0$ in (**a**). Due to measurement limitations, the *z*-directed electric field is only recorded above the singulonic cavity ($z>0$), with values below ($z<0$) extrapolated from symmetry for reference. Solid lines: simulation results; circles: experimental measurements; dashed lines: exponential functions for reference

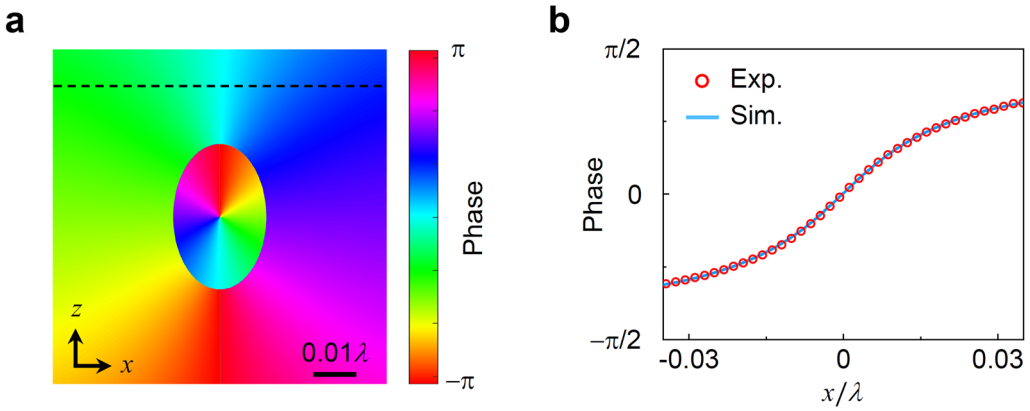

Fig. 4 Simulated and experimentally measured electric field phase distributions near the singularity. **a** Simulated phase distribution of the narwhal-shaped wavefunction in the *x*–*z* plane at $y=0.02\,\lambda$. **b** Comparison of simulated and experimentally measured phases along the dashed line in (**a**)

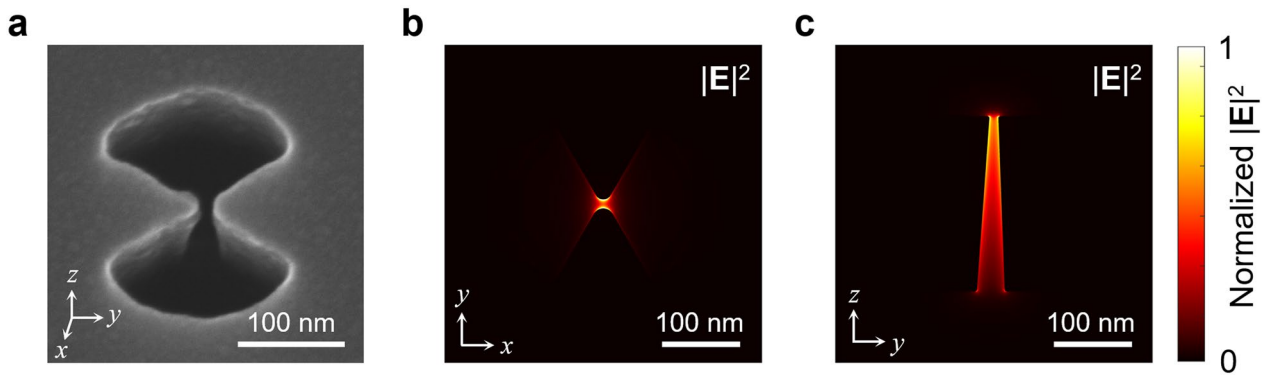

Fig. 5 Singulonic nanocavity operating in the optical regime. **a** SEM image of the central antenna of a fabricated singulonic nanocavity. Simulated electric field distribution in the *x*–*y* plane taken at the height corresponding to the minimum gap ($z=110$ nm) (**b**) and *y*–*z* plane at $x=0$ (**c**)

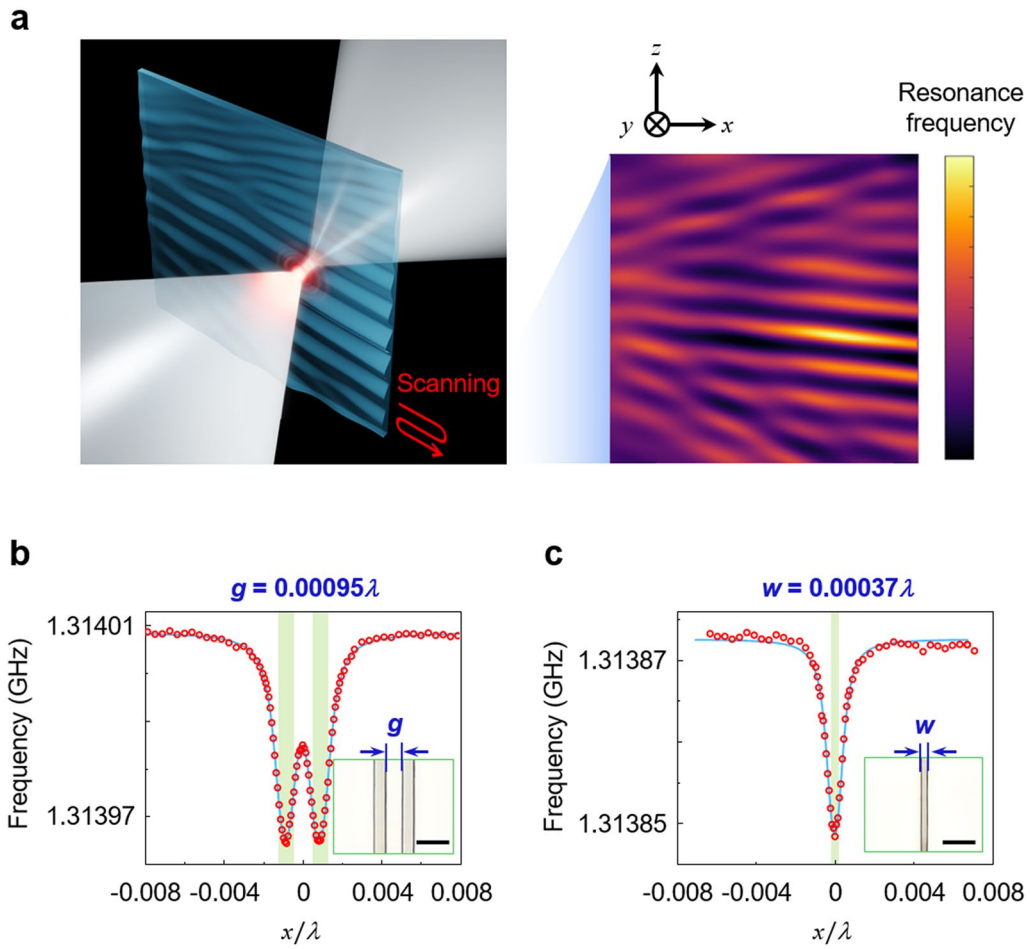

Fig. 6 Schematic and imaging resolution of singular field microscopy. **a** Schematic illustration of singular field microscopy. In this technique, the highly localized singular electric field within a biconical antenna gap acts as a near-field probe, scanning a sample placed in the gap in a plane perpendicular to the antenna's axis. As the sample moves, variations in its material properties within the gap shift the cavity's resonance frequency, thereby revealing topographical features (right panel). **b** Line profile analysis of two closely spaced dielectric polyethylene terephthalate (PET) strips separated by $0.95\times10^{-3}\,\lambda$. Inset: photograph of two strips. **c** Line profile analysis of a dielectric polyethylene terephthalate (PET) strip measuring only $0.37\times10^{-3}\,\lambda$ in width. Inset: photograph of the strip. In (**b**) and (**c**), the circles represent experimental data, the lines indicate fitted curves, and the green-shaded regions show the physical size of the strips. Scalebar: $\lambda/500$

λ^3, and demonstrate that such confinement necessarily arises from a new class of optical eigenmodes—narwhal-shaped wavefunctions—which emerge from the singular dispersion equation and uniquely combine global Gaussian decay with local power-law enhancement. Building on this extreme localization, we introduce singular field microscopy, a near-field imaging technique that employs these singulonic modes as intrinsically localized, background-free light sources, enabling optical imaging with a spatial resolution of $\lambda/1000$.

Looking ahead, the singular dispersion equation provides a powerful and unifying mechanism for achieving lossless, deeply subwavelength field confinement, redefining the fundamental limits of nanophotonic systems. In plasmonics, such confinement is ultimately constrained by three intrinsic mechanisms—ohmic loss, nonlocal effects, and Landau damping—which degrade spatial localization and suppress quality factor. These effects arise from the presence of mobile free electrons: ohmic dissipation stems from resistive currents, nonlocal blurring reflects the delocalized electronic response, and Landau damping results from velocity-matched electronic transitions that irreversibly drain energy from confined photons.

Dielectric media, by contrast, are composed of tightly bound electrons and are inherently free from these limitations. The absence of free carriers eliminates ohmic loss; polarization arises from atomic-scale displacements, suppressing nonlocal effects; and the absence of

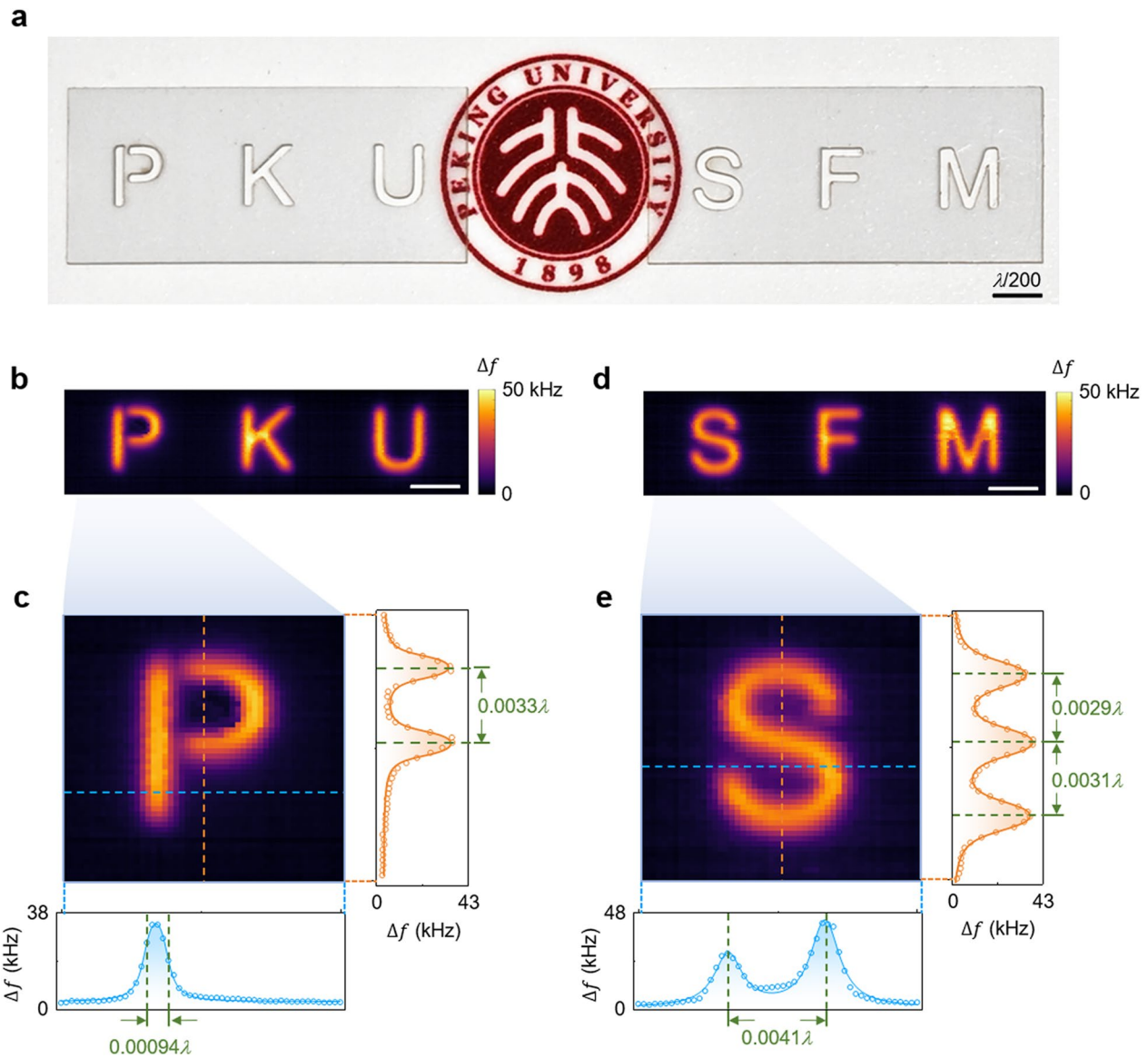

Fig. 7 Imaging arbitrary structures with singular field microscopy. **a** Photographs of two perforated dielectric polyethylene terephthalate (PET) samples patterned with "PKU" and "SFM". **b** Singular field microscopy image of the "PKU" pattern. **c** Line analysis of the imaged "P" pattern, with the bottom and right profiles indicating resonance frequency shifts (Δf) along the horizontal and vertical dashed lines, respectively. **d** Singular field microscopy image of the "SFM" pattern. **e** Line analysis of the imaged "S" pattern, with the bottom and right profiles showing resonance frequency shifts along the horizontal and vertical dashed lines, respectively. Scalebar in (**b**) and (**d**): $\lambda/200$. In (**c**) and (**e**), the circles represent experimental data, the lines indicate fitted curves

available electronic states precludes velocity-matched transitions, eliminating Landau damping. As a result, singulonic structures can support ultra-confined, high-Q optical modes, pushing photonic systems toward atomic-scale dimensions. This unprecedented combination of confinement and coherence lays the physical foundation for a wide range of transformative photonic technologies.

Building on this capability, singular field confinement opens new frontiers across a broad spectrum of applications. In nanophotonic devices, it enables angstrom-scale lasers, light-emitting diodes, electro-optic and all-optical modulators, and photodetectors—paving the way for ultra-compact, energy-efficient photonic integration. In quantum and nonlinear optics, it facilitates Purcell-enhanced emission, single-photon nonlinearities, cavity quantum electrodynamics, and

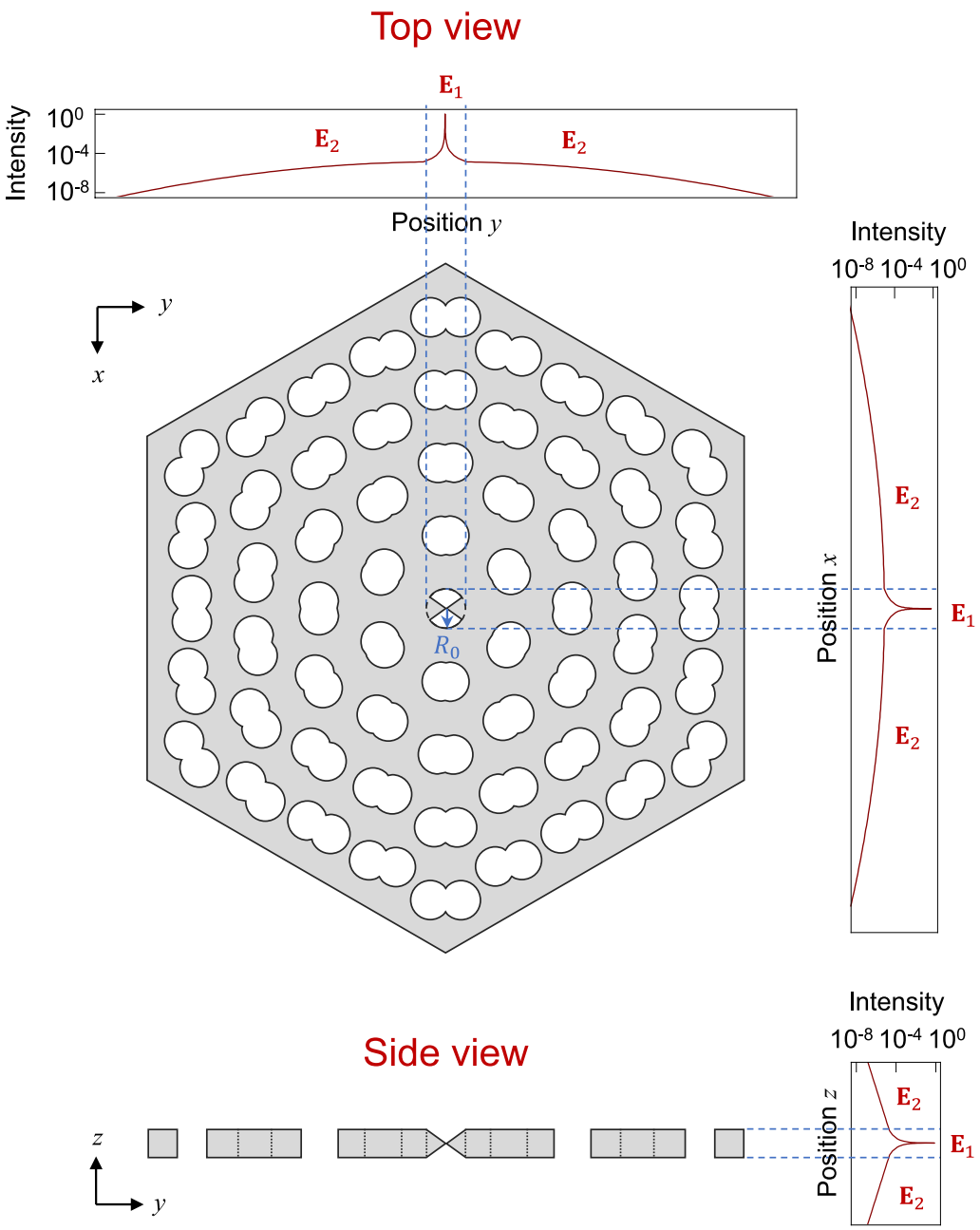

Fig. 8 Singulonic cavity and its narwhal-shaped eigenfunction. A 3D biconical antenna embedded within a twisted lattice cavity forms the singulonic cavity, supporting an eigenmode with a distinctive narwhal-shaped wavefunction in all spatial dimensions. This wavefunction exhibits a power-law divergence at its core (the biconical antenna region, $\mathbf{E}_1$) and a Gaussian-like decaying tail in the twisted-lattice cavity region ($\mathbf{E}_2$)

scalable quantum light sources. In sensing and imaging, it provides intrinsically localized, background-free illumination for atomic-resolution microscopy, ultrasensitive detection, and near-field spectroscopy. Together, these developments define a new regime of singulonics, where the interplay of geometry, material, and dispersion enables transformative control over light–matter interactions at the atomic scale.

4 Methods

4.1 Theoretical analysis of infinite singularity

The singulonic cavity comprises a 3D biconical antenna embedded within a twisted lattice cavity, supporting

eigenmode with a unique narwhal-shaped wavefunction (Fig. 8). These wavefunctions are characterized by a power-law divergence at the core and an exponentially decaying tail, corresponding to the eigenfunctions of the biconical antenna and twisted lattice cavity regions, respectively. The distinct properties of these wavefunctions arise from the dielectric material structures of each region, with their connection at the boundary governed by the boundary conditions.

We begin by solving for the eigenmode in the central biconical antenna region using Maxwell's equations in spherical coordinates (Fig. S16a in the Supplemental Material). In the biconical antenna region, for eigenmodes where the electric field has a singularity at the origin, the electric field energy greatly exceeds the magnetic field energy [22]. As a result, the electric field $\mathbf{E}_1$ is approximately irrotational, and can be described by a potential V. We solve for the potential V separately in both the dielectric and air regions, and connect the solutions through the boundary conditions. Then, by taking the negative gradient of the potential, we can obtain the electric field, which has the following form:

$$\mathbf{E}_1 = C_1 r^{-l} \mathbf{\Theta}(\theta, \varphi), \tag{1}$$

where l is a parameter determined by the structure, $0 < l < 1$, and $\mathbf{\Theta} = (\Theta_x, \Theta_y, \Theta_z)$ is a function of θ and φ (see Theoretical analysis of infinite singularity in Supplemental Material for more details). Here, when $k_0 r$ is significantly smaller than 1, higher-order small terms of the electric and magnetic fields can be neglected.

Notably, the eigenmode exhibits a singularity at the origin, diverging in the form of r^{-l}, which is corresponding to the local power-law field enhancement.

The formation of the infinite electric field singularity arises from the divergence of momentum near the biconical antenna tip. To clearly reveal the wavevector corresponding to the electric field that diverges as a power function at the singularity, we introduce a position-dependent wavevector $\mathbf{k}$ (Fig. S16a in the Supplemental Material):

$$E(r, \theta, \varphi) \equiv \mathrm{e}^{\mathrm{i} \int \mathbf{k}(r,\theta,\varphi) \cdot \mathrm{d}\mathbf{r}}, \tag{2}$$

where all wavevector components diverge as $\frac{1}{r}$ near the singularity (see Theoretical analysis of infinite singularity in Supplemental Material for more details). Further, for any polarization component of the electric field eigenmode, the corresponding wavevector $\mathbf{k} = \mathrm{i}k_r \mathbf{e}_r + k_\theta \mathbf{e}_\theta + k_\varphi \mathbf{e}_\varphi$ satisfies the following dispersion relation:

$$(\mathrm{i}k_r)^2 + k_\theta^2 + k_\varphi^2 - \mathrm{i}\left(\frac{\partial}{\partial r} + \frac{2}{r}\right)(\mathrm{i}k_r) - \mathrm{i}\frac{1}{r}\left(\frac{\partial}{\partial \theta} + \cot\theta\right)k_\theta - \mathrm{i}\frac{1}{r\sin\theta}\frac{\partial}{\partial \varphi}k_\varphi \approx \left(\frac{n\omega}{c}\right)^2. \tag{3}$$

Next, we solve for $\mathbf{E}_2$ in the twisted lattice cavity region. The twisted lattice cavity achieves light field localization through momentum-space mode locking [39, 42]. To analytically derive the eigenmodes of the twisted lattice cavity, its structure can be regarded as a series of gradually varying periodic configurations seamlessly connected (Fig. S17a in the Supplemental Material). At each position within the cavity, the local arrangement can be treated as a unit cell for constructing a corresponding periodic structure. The result shows that the resonance frequencies of the localized modes in the twisted lattice cavity fall within the bandgap of the surrounding structures. This ensures that the electric field is strongly confined to the center of the cavity.

For the periodic structure constructed from the local arrangement, the Hamiltonian can be expressed as:

$$H = \begin{pmatrix} \frac{c}{n_{\mathrm{eff}}} k_1 & \kappa \\ \kappa & \frac{c}{n_{\mathrm{eff}}}(-k_2) \end{pmatrix}, \tag{4}$$

where $k_2 = k_1 - G$, with k_1 and k_2 denoting the wavevectors of the plane waves, and G representing the reciprocal lattice vector of the periodic structure. The parameter $\kappa > 0$ is the coupling coefficient. n_{eff} represents the effective refractive index of the structure. This Hamiltonian results in an energy band (band-edge frequencies: $\omega_\pm$) with a bandgap Δ at the Brillouin zone edge (see Theoretical analysis of infinite singularity in Supplemental Material for more details).

For an electromagnetic wave with a frequency ω within the bandgap, propagation is prohibited, and the wave becomes an evanescent wave in the photonic crystal. Specifically, when $\omega_+ - \omega \ll \Delta$, it forms a decaying standing wave with a wavefunction $\psi = \frac{1}{\sqrt{2}}\begin{pmatrix} 1 \\ 1 \end{pmatrix}$ and wavevectors of

$$k_{\mathrm{evan1,2}} = \pm k_M + \mathrm{i}\frac{n_{\mathrm{eff}}}{c}\sqrt{\Delta(\omega_+ - \omega)}. \tag{5}$$

To simplify the analysis, we first consider a one-dimensional mode with its wavevector along the y-direction and polarization along the x-direction. The corresponding field distribution is

$$\begin{aligned} E(y) &= \tfrac{1}{\sqrt{2}}\left(\mathrm{e}^{\mathrm{i}k_{\mathrm{evan1}}y} + \mathrm{e}^{\mathrm{i}k_{\mathrm{evan2}}y}\right) \\ &= \sqrt{2}\cos\left(k_M y\right)\mathrm{e}^{-\frac{n_{\mathrm{eff}}}{c}\sqrt{\Delta(\omega_+ - \omega)}y}. \end{aligned} \tag{6}$$

In the twisted lattice cavity, both the band-edge frequency and the bandgap exhibit approximately linear variations within the range eigenmode localized (Fig. S17b in the Supplemental Material):

$$\Delta(y) = \Delta_0 + \beta_1 y, \omega_+(y) = \omega_{+0} + \beta_2 y. \tag{7}$$

Different from Eq. (6), the electric field distribution across the entire cavity should be expressed as an integral, in order to account for the spatially varying decay rate of the electromagnetic waves in the cavity:

$$E(y) = \sqrt{2}\cos\left(k_M y\right) \mathrm{e}^{-\int_0^y \mathrm{Im}(k_1(\xi))\mathrm{d}\xi}. \tag{8}$$

For the localized mode at the center of the twisted lattice cavity with a frequency $\omega = \omega_{+0}$, the condition $\omega_+(y) - \omega \ll \Delta(y)$ is approximately satisfied within the mode localized region. When neglecting the parabolic term under the square root, the wavevector of the evanescent wave can be expressed as:

$$k_{\mathrm{evan}1,2}(y) = \pm k_M + \mathrm{i}\frac{n_{\mathrm{eff}}}{c}\sqrt{\Delta_0 \beta_2 y}, \tag{9}$$

then we can derive the electric field distribution,

$$E(y) = \sqrt{2}\cos\left(k_M y\right) \mathrm{e}^{-\frac{2}{3}\frac{n_{\mathrm{eff}}}{c}\sqrt{\Delta_0\beta_2}y^{\frac{3}{2}}}. \tag{10}$$

Further calculations reveal that the band structure exhibits approximate rotational symmetry. Consequently, the electric field propagating along the radial direction with azimuthal polarization can be reasonably approximated with reference to Eq. (10):

$$E_{2\phi}(\rho, \phi) = C_2 f(\phi)\cos\left(k_M \rho\right) \mathrm{e}^{-\nu\rho^{\frac{3}{2}}}, \tag{11}$$

where $\rho = \sqrt{x^2 + y^2}$ is the radial distance, $\phi = \arctan\frac{x}{y}$ is the azimuth angle, and ν is a parameter denoting the confinement of the twisted lattice cavity. $f(\phi)$ represents the azimuthal profile of the electric field.

Our calculations reveal that the localized eigenmode is polarized along the y-direction at the center of the twisted lattice cavity, thus we set $f(\phi) = \sin\phi$ as a reasonable approximation. Then, by decomposing Eq. (11) into its x and y components, we obtain:

$$\begin{cases} E_{2x} = -C_2 \sin\phi\cos\phi\cos\left(k_M\rho\right)\mathrm{e}^{-\nu\rho^{\frac{3}{2}}} \\ E_{2y} = C_2 \sin^2\phi\cos\left(k_M\rho\right)\mathrm{e}^{-\nu\rho^{\frac{3}{2}}} \end{cases}. \tag{12}$$

Notably, this expression indicates that the electric field amplitude along the radial direction has an envelope function resembling a Gaussian one, described as $\mathrm{e}^{-\nu\rho^{\frac{3}{2}}}$.

Finally, the eigenmodes $\mathbf{E}_1$ and $\mathbf{E}_2$ of the biconical antenna and twisted lattice cavity regions are connected using boundary conditions derived from Maxwell's equations. Then, the expression for the dominant electric field component, E_y, is derived as:

$$E_y = C\begin{cases} E_{y0}\left(x^2+y^2+z^2\right)^{-\frac{l}{2}}\Theta_y\left(\frac{y}{\sqrt{x^2+y^2+z^2}}\right) \\ \left(\sqrt{x^2+y^2+z^2} \le R_0\right) \\ \mathrm{e}^{-\nu\left(x^2+y^2\right)^{\frac{3}{4}}}\frac{x^2}{x^2+y^2}\cos\left(k_M\sqrt{x^2+y^2}\right)Z(z) \\ \left(\sqrt{x^2+y^2+z^2} \ge R_0\right) \end{cases}, \tag{13}$$

where C is a normalized constant, and E_{y0} is a structure-dependent parameter. $Z(z)$ represents the wavefunction in the z-direction, which is localized by total internal reflection and thereby decays exponentially outside the cavity.

4.2 Device fabrication

The singulonic cavity, designed for microwave operation, was fabricated via computer-numerically-controlled (CNC) milling. First, high-purity (≥99%) aluminum oxide powder—chosen for its low dielectric loss—was extruded and sintered at elevated temperatures to form a dense ceramic plate. Following a computer-aided design (CAD) pattern, this plate was then CNC-milled into the twisted lattice cavity. In parallel, a 3D biconical antenna was fabricated from high-purity (≥99%) zirconium oxide powder using the same extrusion and sintering process. The achieved radius of curvature at the cone tips is approximately 0.2 mm, as determined by direct measurement. Finally, the antenna was installed into the cavity's central air hole, completing the singulonic cavity assembly. The 0.02 mm air gap was precisely adjusted and calibrated in situ during the experimental setup.

4.3 Experimental characterization

To measure the eigen-wavefunction of the singulonic cavities, we employ a two-port transmission spectroscopy setup with a vector network analyzer, using $|S_{21}|$ signal to extract eigenmode information (Fig. S3 in the Supplemental Material). The excitation antenna, connected to port 1 via a coaxial cable, drives the singulonic cavity's eigenmode in the near field, while a probe antenna on port 2 records the resulting electric field distribution. Within the 0.5–2 GHz measurement range, sampled at 75 kHz intervals, a distinct peak in the transmission spectrum emerges, corresponding to the excited eigenmode. By translating the probe antenna in three dimensions and recording the position-dependent $|S_{21}|$, we obtain the characteristic of the narwhal-shaped eigenwavefunction. Because the direct measurement is influenced by the presence of the probe antenna, we adopted a simulation-assisted correction approach to rigorously account for this effect (Fig. S4 in the Supplemental Material). Specifically, we constructed a full-wave 3D model

that exactly replicates the experimental geometry, including the probe structure. We then computed the eigenmode of the system, and the probe detected eigenmode excited by another antenna.

By comparing the probe detected eigenmode field profile to the measured near-field distribution, we verified excellent agreement—confirming that the simulation accurately captures the experimental perturbation. We then directly compared the simulated eigenmode with the probe detected eigenmode to extract the probe-induced distortion. This differential analysis allowed us to correct for the probe's influence and recover the intrinsic cavity mode profile. The corrected field profiles presented in main text thus reflect the unperturbed mode structure with high fidelity.

Due to measurement limitations, the x-directed electric field near the singularity are measured at $z=0.002\ \lambda$ in x–y plane, the y-directed electric field near the singularity is measured along the side of the biconical antenna in x–y plane at $z=0$. Meanwhile, the z-directed electric field is only recorded above the cavity ($z>0$), with values below ($z<0$) extrapolated from symmetry for reference.

For singular field microscopy, we use one-port reflection spectroscopy to determine the resonance frequency via the $|S_{11}|$ signal (Fig. S12 in the Supplemental Material). A dip in the reflection spectrum, observed between 1.26 and 1.36 GHz at 5 kHz steps, is fitted to identify the resonance frequency. As the sample moves within the air gap, shifts in this measured resonance frequency reveal its topographical features.

4.4 Full-wave simulation

We numerically investigate the eigenmodes of singulonic cavities using 3D full-wave simulations based on the finite-element method using a model that replicates the actual fabricated structure, which includes a finite tip radius and gap size (Fig. S8 in the Supplemental Material). All simulations were performed using COMSOL Multiphysics. The singulonic cavity is embedded in air and enclosed within a perfectly matched layer (PML) to absorb outgoing waves. Scattering boundary conditions were applied at the PML interfaces to minimize artificial reflections and ensure accurate field distribution. These simulations provide key mode characteristics, including field distributions, quality factors, and mode volumes. The dielectric constants are set to 9.6 for aluminum oxide and 29 for zirconium oxide. The mode volume V is calculated as $V=\frac{\int \varepsilon(\mathbf{r})|\mathbf{E}(\mathbf{r})|^2 d^3\mathbf{r}}{\max\left[\varepsilon(\mathbf{r})|\mathbf{E}(\mathbf{r})|^2\right]}$, where $\varepsilon(\mathbf{r})$ is the position-dependent dielectric constant. The quality factor is determined by $Q=\left(\mathrm{Re}[f]\right)/\left(2\mathrm{Im}[f]\right)$, where $\mathrm{Re}[f]$ and $\mathrm{Im}[f]$ represent the real and imaginary parts of the eigenfrequency of the cavity eigenmode.

To assess the influence of fabrication deviations on field confinement, we conducted a comprehensive sensitivity analysis to examine how the mode volume depends on the geometric parameters of the cavity. As shown in Fig. S9 in the Supplemental Material, the mode volume decreases gradually with decreasing tip radius and gap size, and remains well within the deep-subwavelength regime across the range of experimentally realizable parameters.

To evaluate numerical convergence, we performed a mesh sensitivity study using a two-level adaptive refinement strategy near the apex (Fig. S10 in the Supplemental Material). Region 1 spans a broader area around the antenna tip to ensure smooth meshing, while Region 2—the narrow air gap between opposing tips—uses finer mesh elements to resolve the strongly localized fields. The mesh resolution in both regions is controlled by a refinement parameter m, with higher m corresponding to finer meshing.

Figure S11 in the Supplemental Material details the mesh settings as a function of m and shows the resulting mode volume and quality factors. We find that the mode volume converges to $\sim 5\times10^{-7}\ \lambda^3$ for $m\geq 2$ with an air gap of 0.02 mm, and the corresponding quality factor remains stable around $Q\approx 1320$ with further mesh refinement, demonstrating that our simulation results are numerically stable and well-resolved.

Supplementary Information

The online version contains supplementary material available at https://doi.org/10.1186/s43593-025-00104-x.

Additional file 1.

Author contributions

R.-M.M. conceived the concept and supervised the project. W.-Z.M. performed experiments. H.-Y.L. and W.-Z.M. carried out theoretical analysis and numerical simulations. R.-M.M., W.-Z.M. and H.-Y.L. did the data analysis. R.-M.M. wrote the manuscript with input from W.-Z.M. and H.-Y.L.

Funding

This work is supported by National Natural Science Foundation of China (grant nos. 12225402, 12450005, 91950115, 11774014, 62321004, 92250302).

Availability of data and materials

We declare that the data supporting the findings of this study are available within the paper.

Declarations

Competing interests

The authors declare no competing interests.

Received: 10 August 2025 Revised: 23 August 2025 Accepted: 27 August 2025
Published online: 01 October 2025

References

1. P.A.M. Dirac, The quantum theory of the emission and absorption of radiation. Proc. R. Soc. Lond. A **114**, 243 (1927)
2. E.M. Purcell, Spontaneous emission probabilities at radio frequencies. Phys. Rev. **69**, 681 (1946)
3. K.J. Vahala, Optical microcavities. Nature **424**, 839 (2003)
4. S. Haroche, Nobel lecture: controlling photons in a box and exploring the quantum to classical boundary. Rev. Mod. Phys. **85**, 1083 (2013)
5. A.F. Kockum, A. Miranowicz, S. De Liberato, S. Savasta, F. Nori, Ultrastrong coupling between light and matter. Nat. Rev. Phys. **1**, 19 (2019)
6. P. Forn-Díaz, L. Lamata, E. Rico, J. Kono, E. Solano, Ultrastrong coupling regimes of light–matter interaction. Rev. Mod. Phys. **91**, 025005 (2019)
7. W.L. Barnes, A. Dereux, T.W. Ebbesen, Surface plasmon subwavelength optics. Nature **424**, 824 (2003)
8. E. Ozbay, Plasmonics: merging photonics and electronics at nanoscale dimensions. Science **311**, 189 (2006)
9. J.N. Anker, W.P. Hall, O. Lyandres, N.C. Shah, J. Zhao, R.P. Van Duyne, Biosensing with plasmonic nanosensors. Nat. Mater. **7**, 442 (2008)
10. J.A. Schuller, E.S. Barnard, W. Cai, Y.C. Jun, J.S. White, M.L. Brongersma, Plasmonics for extreme light concentration and manipulation. Nat. Mater. **9**, 193 (2010)
11. H.A. Atwater, A. Polman, Plasmonics for improved photovoltaic devices. Nat. Mater. **9**, 205 (2010)
12. D.K. Gramotnev, S.I. Bozhevolnyi, Plasmonics beyond the diffraction limit. Nat. Photon. **4**, 83 (2010)
13. Y. Liu, X. Zhang, Metamaterials: a new frontier of science and technology. Chem. Soc. Rev. **40**, 2494 (2011)
14. O. Hess, J.B. Pendry, S.A. Maier, R.F. Oulton, J.M. Hamm, K.L. Tsakmakidis, Active nanoplasmonic metamaterials. Nat. Mater. **11**, 573 (2012)
15. M. Kauranen, A.V. Zayats, Nonlinear plasmonics. Nat. Photonics **6**, 737 (2012)
16. M.S. Tame, K.R. McEnery, Ş.K. Özdemir, J. Lee, S.A. Maier, M.S. Kim, Quantum plasmonics. Nat. Phys. **9**, 329 (2013)
17. J.B. Khurgin, How to deal with the loss in plasmonics and metamaterials. Nat. Nanotechnol. **10**, 2 (2015)
18. K.L. Tsakmakidis, O. Hess, R.W. Boyd, X. Zhang, Ultraslow waves on the nanoscale. Science **358**, eaan5196 (2017)
19. R.M. Ma, R.F. Oulton, Applications of nanolasers. Nat. Nanotechnol. **14**, 12 (2019)
20. J.J. Baumberg, J. Aizpurua, M.H. Mikkelsen, D.R. Smith, Extreme nanophotonics from ultrathin metallic gaps. Nat. Mater. **18**, 668 (2019)
21. T. Wu, M. Gurioli, P. Lalanne, Nanoscale light confinement: the Q's and V's. ACS Photonics **8**, 1522 (2021)
22. Y.H. Ouyang, H.Y. Luan, Z.W. Zhao, W.Z. Mao, R.M. Ma, Singular dielectric nanolaser with atomic-scale field localization. Nature **632**, 287 (2024)
23. Y. Zhang, M. Lončar, Submicrometer diameter micropillar cavities with high quality factor and ultrasmall mode volume. Opt. Lett. **34**, 902 (2009)
24. S. Hu, S.M. Weiss, Design of photonic crystal cavities for extreme light concentration. ACS Photonics **3**, 1647 (2016)
25. H. Choi, M. Heuck, D. Englund, Self-similar nanocavity design with ultrasmall mode volume for single-photon nonlinearities. Phys. Rev. Lett. **118**, 223605 (2017)
26. S. Hu, M. Khater, R. Salas-Montiel, E. Kratschmer, S. Engelmann, W.M.J. Green, S.M. Weiss, Experimental realization of deep-subwavelength confinement in dielectric optical resonators. Sci. Adv. **4**, eaat2355 (2018)
27. M. Albrechtsen, B. Vosoughi Lahijani, R.E. Christiansen, V.T.H. Nguyen, L.N. Casses, S.E. Hansen, N. Stenger, O. Sigmund, H. Jansen, J. Mørk, S. Stobbe, Nanometer-scale photon confinement in topology-optimized dielectric cavities. Nat. Commun. **13**, 6281 (2022)
28. A.N. Babar, T.A.S. Weis, K. Tsoukalas, S. Kadkhodazadeh, G. Arregui, B. Vosoughi Lahijani, S. Stobbe, Self-assembled photonic cavities with atomic-scale confinement. Nature **624**, 57 (2023)
29. R.M. Ma, Nanolaser technology with atomic-scale field localization. Nat. Rev. Electr. Eng. **1**, 632 (2024)
30. J.B. Pendry, L. Martin-Moreno, F.J. Garcia-Vidal, Mimicking surface plasmons with structured surfaces. Science **305**, 847 (2004)
31. N. Fang, H. Lee, C. Sun, X. Zhang, Sub-diffraction-limited optical imaging with a silver superlens. Science **308**, 534 (2005)
32. K.L. Tsakmakidis, A.D. Boardman, O. Hess, 'Trapped rainbow' storage of light in metamaterials. Nature **450**, 397 (2007)
33. R.F. Oulton, V.J. Sorger, T. Zentgraf, R.M. Ma, C. Gladden, L. Dai, G. Bartal, X. Zhang, Plasmon lasers at deep subwavelength scale. Nature **461**, 629 (2009)
34. A.E. Miroshnichenko, S. Flach, Y.S. Kivshar, Fano resonances in nanoscale structures. Rev. Mod. Phys. **82**, 2257 (2010)
35. A.I. Kuznetsov, A.E. Miroshnichenko, M.L. Brongersma, Y.S. Kivshar, B. Luk'yanchuk, Optically resonant dielectric nanostructures. Science **354**, aag2472 (2016)
36. L. Feng, R. El-Ganainy, L. Ge, Non-hermitian photonics based on parity–time symmetry. Nat. Photonics **11**, 752 (2017)
37. T. Ozawa, H.M. Price, A. Amo, N. Goldman, M. Hafezi, L. Lu, M.C. Rechtsman, D. Schuster, J. Simon, O. Zilberberg, I. Carusotto, Topological photonics. Rev. Mod. Phys. **91**, 015006 (2019)
38. H.Z. Chen, T. Liu, H.Y. Luan, R.J. Liu, X.Y. Wang, X.F. Zhu, Y.B. Li, Z.M. Gu, S.J. Liang, H. Gao, L. Lu, L. Ge, S. Zhang, J. Zhu, R.M. Ma, Revealing the missing dimension at an exceptional point. Nat. Phys. **16**, 571 (2020)
39. X.R. Mao, Z.K. Shao, H.Y. Luan, S.L. Wang, R.M. Ma, Magic-angle lasers in nanostructured moiré superlattice. Nat. Nanotechnol. **16**, 1099 (2021)
40. C. Wang, Z. Fu, W. Mao, J. Qie, A.D. Stone, L. Yang, Non-hermitian optics and photonics: from classical to quantum. Adv. Opt. Photon. **15**, 442 (2023)
41. H.Y. Luan, Y.H. Ouyang, Z.W. Zhao, W.Z. Mao, R.M. Ma, Reconfigurable moiré nanolaser arrays with phase synchronization. Nature **624**, 282 (2023)
42. R.M. Ma, H.Y. Luan, Z.W. Zhao, W.Z. Mao, S.L. Wang, Y.H. Ouyang, Z.K. Shao, Twisted lattice nanocavity with theoretical quality factor exceeding 200 billion. Fundam. Res. **3**, 537 (2023)
43. S.T. Ha, Q. Li, J.K.W. Yang, H.V. Demir, M.L. Brongersma, A.I. Kuznetsov, Optoelectronic metadevices. Science **386**, eadm7442 (2024)
44. J.M. Raimond, M. Brune, S. Haroche, Manipulating quantum entanglement with atoms and photons in a cavity. Rev. Mod. Phys. **73**, 565 (2001)
45. S. Gleyzes, S. Kuhr, C. Guerlin, J. Bernu, S. Deléglise, U.B. Hoff, M. Brune, J.-M. Raimond, S. Haroche, Quantum jumps of light recording the birth and death of a photon in a cavity. Nature **446**, 297 (2007)
46. C.-Y. Lu, J.-W. Pan, Quantum-dot single-photon sources for the quantum internet. Nat. Nanotechnol. **16**, 1294 (2021)
47. J.B. Khurgin, G. Sun, Comparative analysis of spasers, vertical-cavity surface-emitting lasers and surface-plasmon-emitting diodes. Nat. Photonics **8**, 468 (2014)
48. J.B. Khurgin, Ultimate limit of field confinement by surface plasmon polaritons. Faraday Discuss. **178**, 109 (2015)
49. B. Hecht, B. Sick, U.P. Wild, V. Deckert, R. Zenobi, O.J.F. Martin, D.W. Pohl, Scanning near-field optical microscopy with aperture probes: fundamentals and applications. J. Chem. Phys. **112**, 7761 (2000)
50. X. Chen, D. Hu, R. Mescall, G. You, D.N. Basov, Q. Dai, M. Liu, Modern scattering-type scanning near-field optical microscopy for advanced material research. Adv. Mater. **31**, 1804774 (2019)
51. R. Hillenbrand, Y. Abate, M. Liu, X. Chen, D.N. Basov, Visible-to-THz near-field nanoscopy. Nat. Rev. Mater. **10**, 285 (2025)
52. Z. Zhao, V. Kravtsov, Z. Wang, Z. Zhou, L. Dou, D. Huang, Z. Wang, X. Cheng, M.B. Raschke, T. Jiang, Applications of ultrafast nano-spectroscopy and nano-imaging with tip-based microscopy. eLight (2025). https://doi.org/10.1186/s43593-024-00079-1